Open access • Journal Article • DOI:10.1029/95JC00305

Tropical instability wave kinematics: Observations from the Tropical Instability Wave Experiment — Source link

L. Qiao, Robert H. Weisberg

Published on: 15 May 1995 - Journal of Geophysical Research (John Wiley & Sons, Ltd)

Topics: Tropical instability waves, Equatorial waves, Tropical wave, Wind wave and Wave propagation

5-15-1995

Tropical Instability Wave Kinematics: Observations from the Tropical Instability Wave Experiment

L. Qiao
University of South Florida

Robert H. Weisberg
University of South Florida, weisberg@marine.usf.edu

JOURNAL OF GEOPHYSICAL RESEARCH, VOL. 100, NO. C5, PAGES 8677–8693, MAY 15, 1995

Tropical instability wave kinematics: Observations from the Tropical Instability Wave Experiment

L. Qiao and R. H. Weisberg
Department of Marine Science, University of South Florida, St. Petersburg

Abstract. The kinematics of planetary waves originating from instability of the near-surface equatorial currents are reported on using velocity measurements from an array of acoustic Doppler current profilers deployed in the equatorial Pacific during the Tropical Instability Wave Experiment. A distinctive wave season was observed from August to December 1990, with wave energy confined primarily above the core of the Equatorial Undercurrent. Particle motions in the horizontal plane are described by eccentric ellipses oriented toward the north, but tilting into the cyclonic shear of the South Equatorial Current. The tilt is maximum near the surface just north of the equator and decreases to the south and with depth. The distribution of wave variance is narrowband in both frequency and zonal wavenumber, with central period, zonal wavelength, and westward directed phase propagation estimated to be 500 hours, 1060 km, and 59 cm s^{-1}, respectively. Neither the meridional nor the vertical wavenumber component is statistically different from zero. These results generally agree with previous findings on tropical instability waves from the Atlantic and Pacific Oceans, and, in the undersampled arena of geophysical measurements, they provide an example where statistical inference is supported by an ensemble of independent measurements.

1. Introduction

The near-surface circulations of the equatorial Atlantic and Pacific Oceans may be described by a westward flowing South Equatorial Current (SEC) within the surface layer above an eastward flowing Equatorial Undercurrent (EUC) within the thermocline. These currents vary seasonally with the trade winds that force them. Generally, as the southeast trade winds intensify from their boreal springtime minimum, the SEC accelerates until a zonal pressure gradient is established to balance the wind stress. Prior to achieving this balance the equatorial currents become unstable, generating waves of planetary scale. Such wave observations, reported from the Global Atmospheric Research Program (GARP) Atlantic Tropical Experiment (GATE) by *Düing et al.* [1975], motivated a set of stability analyses by *Philander* [1976, 1978]. Similar waves were reported in the Pacific by *Legeckis* [1977]. While seasonally and interannually modulated, these tropical instability waves are now recognized as ubiquitous features of the tropical circulation field. Initial studies of their interactions with the background fields using in situ data from the Atlantic and Pacific Oceans by *Weisberg* [1984] and *Hansen and Paul* [1984], respectively, showed that these waves play important roles in the near-surface heat and momentum balances, confirming inferences drawn from the numerical model study of *Cox* [1980].

With the objective of further defining the effects of these waves on the near-surface mass, momentum, heat, and mechanical energy balances, the Tropical Instability Wave Experiment (TIWE) was initiated in boreal spring 1990 near 140°W. The TIWE field program included arrays of moored instrumentation, shipboard hydrographic mapping, and Lagrangian drifter tracking. Reported herein are velocity observations from an equatorial array of subsurface moored, acoustic Doppler current profilers (ADCP) centered on 0°, 140°W. Specific focus is on a description of the background currents, the observed variability, and the wave's kinematics. Mass, momentum, and energy considerations will be topics of future correspondence. Section 2 reviews previous instability wave observations. Section 3 introduces the field program and the data. Section 4 describes the instability wave variance, as observed by the equatorial array, and section 5 provides a wavenumber analysis. The results are discussed in section 6, where the available evidence suggests a hypothesis on the roles of the SEC and the EUC in tropical instability wave generation.

Paper number 95JC00305.
0148-0227/95/95JC-00305$05.00

2. Background

Tropical instability wave observations have been reported by a variety of means. These include (1) velocity measurements from moorings [*Weisberg*, 1979; *Weisberg et al.*, 1979a; *Halpern et al.*, 1983; *Weisberg*, 1984; *Philander et al.*, 1985; *Lukas*, 1987; *Weisberg et al.*, 1987; *Halpern et al.*, 1988; *Weisberg and Weingartner*, 1988; *Halpern*, 1989; *Bryden and Brady*, 1989; *Weingartner and Weisberg*, 1991], drifters [*Hansen and Paul*, 1984; *Reverdin and McPhaden*, 1986], and shipboard profilers [*Düing et al.*, 1975; *Wilson and Leetmaa*, 1988; *Luther and Johnson*, 1990]; (2) sea surface temperature (SST) measurements from satellite advanced very high resolution radiometer (AVHRR) imagery [*Legeckis*, 1977; *Brown*, 1979; *Legeckis et al.*, 1983; *Legeckis*, 1986; *Legeckis and Reverdin*, 1987; *Pullen et al.*, 1987; *Steger and Carton*, 1991] and volunteer observing ships [*Mayer et al.*, 1990]; (3) sea level measurements from tide gauges [*Wyrtki*, 1978; *Mitchum and Lukas*, 1987], satellite altimetry [*Malardé et al.*, 1987; *Musman*, 1989; *Périgaud*, 1990], and inverted echo sounders [*Miller et al.*, 1985];

Table 1. A Summary of Period, Wavelength, and Phase Speed Estimates Made for Tropical Instability Waves

Reference	Period, days	Wavelength, km	Phase Speed, cm s^{-1}
Model Predictions			
Philander [1976]	40	900/2000	
Philander [1978]	30	1100	
Cox [1980]	34	1000	
Philander et al. [1986]	21–28	1000	
McCreary and Yu [1992]	21	785	
Velocity Measurements			
Düing et al. [1975]	16–21	2600	−190
Harvey and Patzert [1976]	25	1000	−50
Weisberg et al. [1979a]	31	990–1220	
Weisberg et al. [1979b]*	16	1200	−80
Weisberg [1979]	16/32	760–1250	−27 to −65
Luyten and Roemmich [1982]*	26	1400	
Weisberg [1984]	25	1140	−53
Philander et al. [1985]	21	1000	
Eriksen and Richman [1988]*	9–45	<4000	
Halpern et al. [1988]	20	1320–1600	−81 to −93
Weisberg and Weingartner [1988]	25	1000–1200	−50 to −55
Wilson and Leetmaa [1988]	20–30	1000	−27
Sea Surface Temperature Measurements			
Legeckis [1977]	25	1000	
Legeckis et al. [1983]	25	1000	
Legeckis [1986]	25	600–1200	−21 to −49
Legeckis and Reverdin [1987]	24	1000	
Pullen et al. [1987]	25	1000	
Mayer et al. [1990]	21–37	825–1924	−50
Sea Level Measurements			
Wyrtki [1978]	34	1100	
Miller et al. [1985]	20–80	1000	
Périgaud [1990]	28–40	1000–2000	

Included are papers with wavelength or phase speed estimates.
*These results are from current meter measurements below the thermocline.

and (4) salinity measurements from shipboard conductivity-temperature-depth (CTD) profiles [*Düing et al.*, 1975]. The subsurface expression of these instability waves by energy propagation into the abyss has also been reported by *Harvey and Patzert* [1976], *Weisberg et al.* [1979b], *Weisberg and Horigan* [1981], *Luyten and Roemmich* [1982], and *Eriksen and Richman* [1988]. Many of these references provide estimates of zonal wavenumber and phase speed (Table 1) that generally show westward propagating waves with period, zonal wavelength, and phase speed centered about 3 weeks, 1000 km, and 50 cm s^{-1}, respectively.

The tropical instability waves appear to be confined mainly to the surface layer, with energy dropping precipitously through the thermocline. Thus, on the equator, most of the wave energy, primarily in the form of perturbation kinetic energy, appears above the EUC core [*Weisberg*, 1979, 1984; *Philander et al.* 1985; *Halpern et al.*, 1988; *Weisberg and Weingartner*, 1988; *Luther and Johnson*, 1990]. Below the EUC core a spectral shift to slightly lower frequency is also observed [*Weisberg*, 1979; *Philander et al.*, 1985; *Halpern et al.*, 1988].

The instability waves are seasonally modulated, apparently in relationship to the westward flowing SEC [e.g., *Halpern et al.*, 1988]. Since the SEC is related to the intensity of the southeast trade winds and the zonal pressure gradient tending to balance these winds, the duration of the instability wave season differs between the Pacific and Atlantic Oceans [*Legeckis*, 1986; *Halpern and Weisberg*, 1989]. *Weisberg and Weingartner* [1988] attributed the relatively short wave season in the Atlantic to the linear adjustment time of the zonal pressure gradient. The instability waves may therefore be characterized as nonlinear features modulated by linear processes, with their importance stemming from their nonlinear interactions with the background fields, as shown in previous studies.

Positive deformation work within the cyclonic shear of the EUC was implied from short-duration measurements below the EUC core [*Weisberg et al.*, 1979a]. Near-surface measurements were reported from the Seasonal Response of the Equatorial Atlantic (SEQUAL) Experiment by *Weisberg* [1984] using moored current meters and from the Pacific Ocean by *Hansen and Paul* [1984] using surface drifters. *Weisberg* [1984] found that the onset of large horizontal Reynolds stress values occurred synchronously with the instability waves and that the deformation work (barotropic conversion) calculated within the surface cyclonic shear region of the SEC just north of the equator was sufficient to account for the instability wave's growth. Both the Reynolds stress and the wave perturbation energy decreased below 50 m depth. Wave energy was also found to progress eastward, opposite to the direction of phase propagation.

Hansen and Paul [1984], with data covering a broad latitudinal extent, showed that the largest barotropic conversion of mean to wave energy at the surface occurred within the SEC. Their observations implied that the waves extract energy from the mean flow just to the north of and, conversely, just to the south of the equator and that the instability waves cause heat to converge on the equator, opposing the cooling effects of Ekman divergence. The Reynolds stress analysis of *Lukas* [1987] further supported the idea of near-surface barotropic production just north of the equator.

While the near-surface horizontal Reynolds stresses associated with the instability waves in both the Atlantic and Pacific Oceans have been found to be largest on, with oppositely directed stress gradients to the north and south of, the equator, the Reynolds stress gradients alone do not imply an interaction between the background currents and the waves [*Charney and Drazin*, 1961], since the Reynolds stress divergence may be balanced by a Coriolis force related to a stress-induced meridional circulation. Using the SEQUAL data, *Weisberg and Weingartner* [1988] investigated the *Eliasen and Palm* [1960] flux vector divergence between the equator and 0.75°N and 0.75°S and found that the waves decelerate the SEC to the north of the equator and accelerate it to the south. Thus the instability waves tend to remove the negative near-surface shear (cyclonic, north of

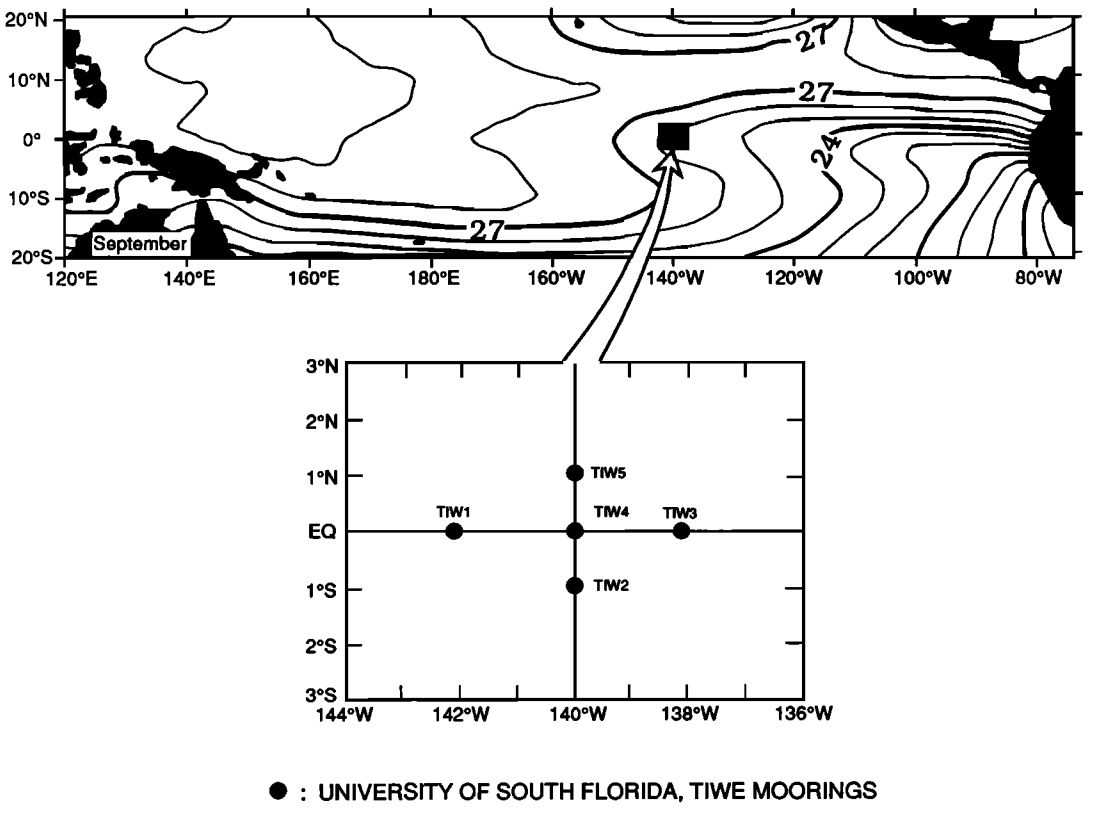

Figure 1. The location of the Tropical Instability Wave Experiment (TIWE) equatorial array in relation to the tropical Pacific Ocean's climatological sea surface temperature distribution for September (courtesy of M. McCarty and M. J. McPhaden, National Oceanic and Atmospheric Administration/Pacific Marine Environmental Laboratory (NOAA/PMEL)).

the equator). This finding, along with the associated energy balance on the equator and the distributions of the Reynolds fluxes observed off the equator at 1.75°N, 3°N, and 6°N, led to the conclusion that the instability waves in the Atlantic gain their energy through barotropic instability within the cyclonic shear region of the SEC just north of the equator. The Reynolds temperature flux distributions also supported the heat transport argument of *Hansen and Paul* [1984]. Additional support for the near-surface confinement of the horizontal Reynolds stress was given by *Wilson and Leetmaa* [1988].

Using repeated meridional sections of velocity and density from the Hawaii to Tahiti Shuttle Experiment, *Luther and Johnson* [1990] provided further insights on the instability mechanisms. Three distinct sources of wave energy were identified, the first being the barotropic mechanism described earlier, but with emphasis on the shear region between the EUC at the equator and the SEC north of the equator, and the other two being baroclinic mechanisms occurring at the frontal regions between 3°N–6°N and 5°N–9°N, respectively. The timing of these mechanisms differed from one another, the first occurring in boreal summer/fall and the other two occurring in winter and spring, respectively. Instabilities deriving from these different mechanisms were suggested as accounting for the differences in the observed periods of oscillation.

There have been remarkable agreements between tropical instability wave observations and numerical model simulations [e.g., *Philander et al.*, 1986]. Recent progress on the mechanisms and regions of generation has been made by *McCreary and Yu* [1992] and *Yu* [1992], clarifying the importance of the cyclonic shear region of the SEC/EUC and the relative unimportance of the North Equatorial Countercurrent and introducing a new frontal instability mechanism related to the strong meridional temperature gradient in the surface layer north of the equator.

3. Field Program and Data

The TIWE equatorial array consisted of five subsurface moorings, each with an RD Instruments, Inc., 150-kHz ADCP and a Sea-Bird Electronics, Inc., SEACAT conductivity, temperature, and depth recorder. The moorings, designated TIW1, TIW2, TIW3, TIW4, and TIW5, were deployed in a diamond-shaped array nominally centered upon 0°, 140°W (Figure 1). The mooring locations, record durations, and nominal instrument depths are listed in Table 2. A 100% data return was achieved, with the ADCPs providing vertical profiles of horizontal velocity vectors and the SEACATs providing for vertical positioning and sound speed corrections. The moorings were stable, with vertical excursions of only a few meters. Upon correcting for the sound speed at the transducers and for the mean ambient sound speed between the transducers and the surface [e.g., *Johns*, 1988], hourly velocity data from May 12, 1990, to June 18, 1991, were resampled by linear interpolation at 10-m intervals between 250 and 30 m.

An example of the hourly sampled meridional v velocity

Table 2. TIWE Equatorial Array Mooring Positions, Record Lengths, and Instrument Depths

Mooring	Latitude, Longitude Position	Record Length, hours	Instrument Depth, m
TIW1	0°0.14'N, 141°50.6'W	9737	273.6
TIW2	0°57.8'S, 139°57.5'W	9667	280.5
TIW3	0°02.4'N, 137°57.7'W	9689	281.5
TIW4	0°03.2'S, 140°08.4'W	9713	276.5
TIW5	1°01.5'N, 139°57.4'W	9761	266.4

Record lengths begin on May 12, 1990, 0000 UT.

component from TIW4 at 30 m depth is shown in Figure 2. From August through December, regular oscillations are observed, with amplitude exceeding 50 cm s^{-1} and periodicity of about 3 weeks. These seasonally modulated, narrow frequency band, primarily v component oscillations are the tropical instability waves. After the abrupt end of the wave season the oscillations are smaller and with broader bandwidth.

The distributions with time, depth, and latitude (1°N to 1°S along 140°W) of the u and v component oscillations are shown in Figures 3 and 4, respectively. For this purpose the data were low-pass-filtered (using a truncated Fourier transform) to exclude oscillations at timescales shorter than 10 days, and the values at depths shallower than 30 m were estimated by linear extrapolation using the vertical shear between 40 and 30 m (the extrapolation is supported by the findings of *McPhaden et al.* [1991]). The u component isotachs are representative of the zonally oriented currents found near the equator. Specifically, there is a highly variable, near-surface confined SEC overriding the EUC with its high-speed core located near the top of the thermocline (Figure 5). Discussions of these currents from long-term current meter records at this location are given by *Halpern et al.* [1988], *McPhaden and Taft* [1988], and *Halpern and Weisberg* [1989]. Of the three latitudes sampled the EUC is maximum on and nearly symmetric about the equator, while the SEC is maximum to the north of the equator. The primary variations in the EUC appear to be both annual and intraseasonal. Three major events of maximum EUC transport are observed. During July 1990 and April 1991 the EUC was shallow in contrast to December 1990, when it was deeper. The former two maxima coincide with the annual cycle of the southeast trade winds which, with varying phase, tend to be weakest over the eastern half of the equatorial Pacific in boreal spring [e.g., *Meyers*, 1979; *Mitchell and Wallace*, 1992], causing a concomitant eastward acceleration of the near-surface currents by the eastward directed zonal pressure gradient force. This is in contrast to wintertime maxima that occur in response to bursts of westerly winds over the far western portion of the equatorial Pacific [e.g., *McPhaden and Taft*, 1988]. In agreement with previous studies the SEC is observed to be most developed from August to December 1990, in between the first two EUC maxima, and again from February to April 1991, in between the second two EUC maxima. Other than those two periods the SEC appears to be relatively weak, and westward flow was even absent on the equator from April to June 1991. The SEC is also observed to penetrate deeper both to the north and south of the equator than on the equator and to be strongest at the 1°N location.

In contrast to u, the v component consists of seasonally modulated, higher-frequency oscillations. In particular, a series of regular, large-amplitude oscillations are observed at all of the sample locations beginning in August 1990 and lasting into December 1990. This instability wave season for the TIWE began with the seasonal acceleration of the SEC and ended with a wintertime pulse of eastward momentum (that propagated as a Kelvin wave from the western Pacific) which temporarily halted the SEC. The v component oscillations during the wave season are largest on the equator and within the westward flowing SEC, with amplitudes decreasing across the thermocline to relatively small values at or below the EUC core.

Philander et al. [1985] and *Halpern et al.* [1988] observed the instability waves to be energetic and regular when the surface flow was westward and absent when the flow was eastward. The TIWE observations are similar in that the instability wave season ended in December 1990 with the appearance of an EUC maximum at that time. Subsequently, while the SEC reformed, the instability waves did not, suggesting that westward flow locally is not a sufficient condition for instability. *Luther and Johnson* [1990] also made this point and suggested that a strongly developed EUC is also necessary.

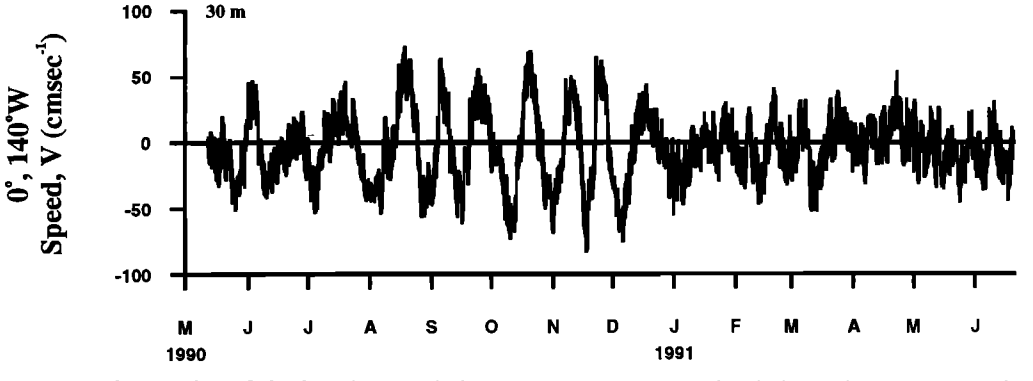

Figure 2. Time series of the hourly sampled v component at 30 m depth from the TIW4 mooring.

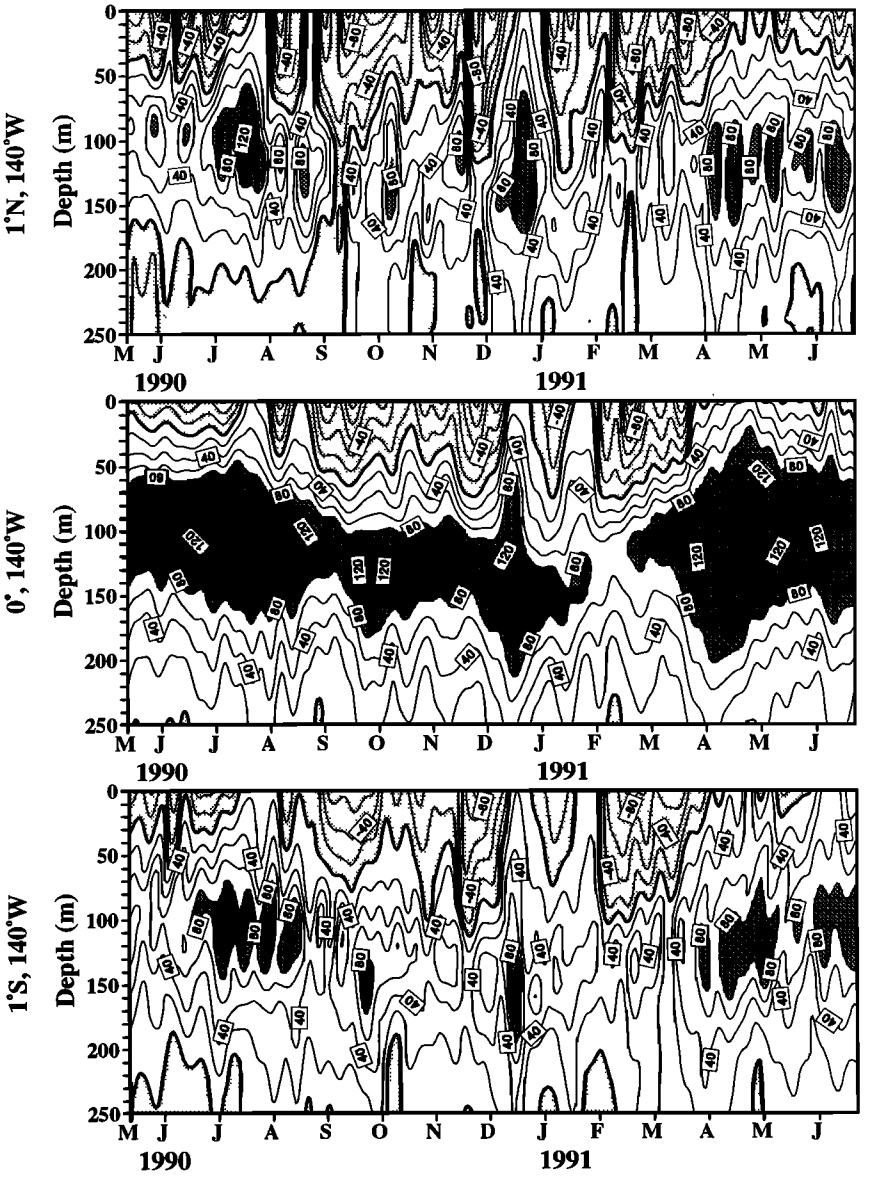

Figure 3. The u component as a function of deptn and time at moorings TIW2, TIW4, and TIW5, low-pass-filtered to exclude fluctuations at timescales shorter than 10 days. Westward flow is denoted by light stippling, eastward flows faster than 80 cm s^{-1} are denoted by dark stippling, and the contour interval is 20 cm s^{-1}.

4. Variance Distribution and Modulation

Variance density spectra for the v and u components support the description of the instability waves as narrow-band, primarily v component processes. Figure 6 shows the logarithm of these spectral densities as functions of depth and frequency along 140°W at 1°N, 0°, and 1°S. The highlighted values show a peak in the v component centered on 500-hour periodicity, nearly symmetric about the equator and confined above the EUC core (located at 110 m, on average). On the equator there is a subtle suggestion of a shift to slightly lower frequency with depth. While this shift is not statistically significant, it is consistent with previous observations (section 2). The u component spectra do not show a similar spectral peak. Instead, the variance density increases with decreasing frequency, except for local maxima about the EUC core at both 1°N and 1°S. These local maxima are consistent with meridional advection in the presence of the EUC mean meridional shear, as will be commented upon later.

The kinematics of the velocity component oscillations may be described using a rotary spectral analysis. Figure 7 shows the semiminor to semimajor axes ratio for the velocity hodograph ellipse and the ellipse polarization as a function of frequency and depth along 140°W at 1°N, 0°, and 1°S. On the equator the motions tend to be rectilinear without preferred polarization, while off the equator the ellipse eccentricity decreases and the oscillations tend to be polarized clockwise to the north and anticlockwise to the south, respectively. Similar findings, consistent with equatorial wave dynamics, have been reported for the equatorial Atlantic and Pacific

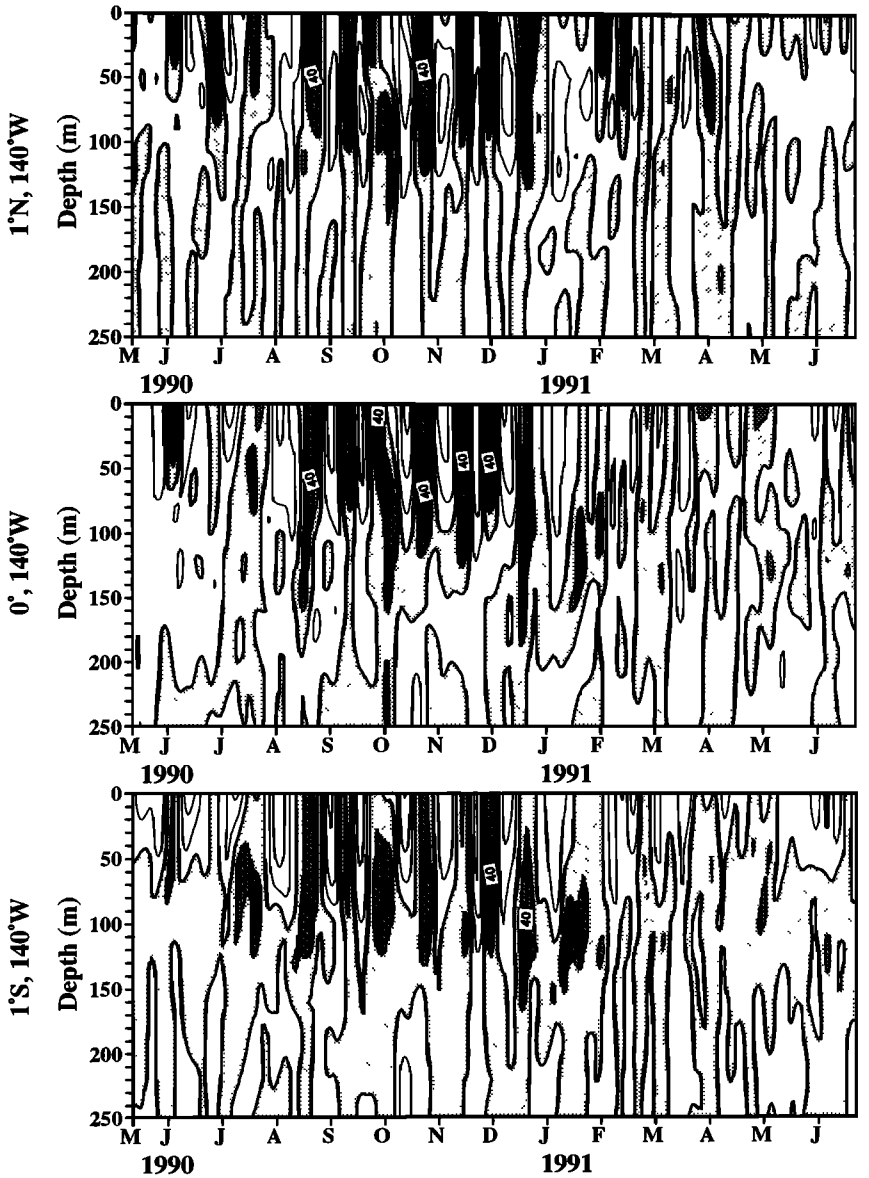

Figure 4. The v component as a function of depth and time at moorings TIW2, TIW4, and TIW5, low-pass-filtered to exclude fluctuations at timescales shorter than 10 days. Northward flow is stippled, southward flow is open, and the contour interval is 20 cm s^{-1}.

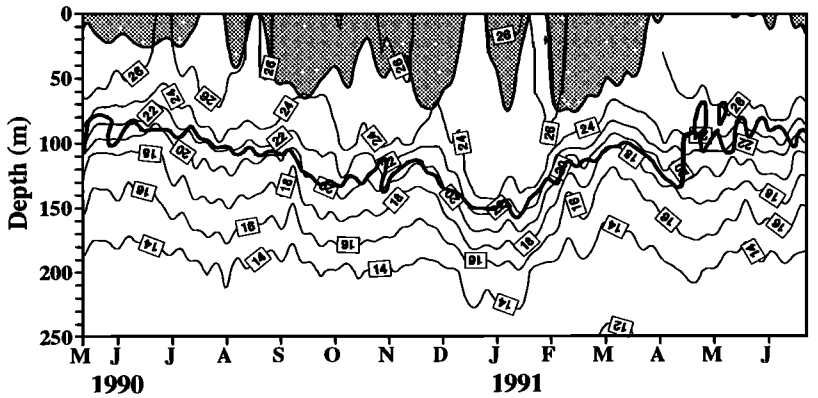

Figure 5. Isotherm depths as a function of time from a Tropical Ocean and Global Atmosphere-Tropical Atmosphere Ocean (TOGA-TAO) array mooring at 0°, 140°W (courtesy of M. J. McPhaden, NOAA/PMEL) upon which are superimposed the EUC core depth, defined by $\partial u/\partial z = 0$, and the region of the westward flowing SEC, denoted by stippling.

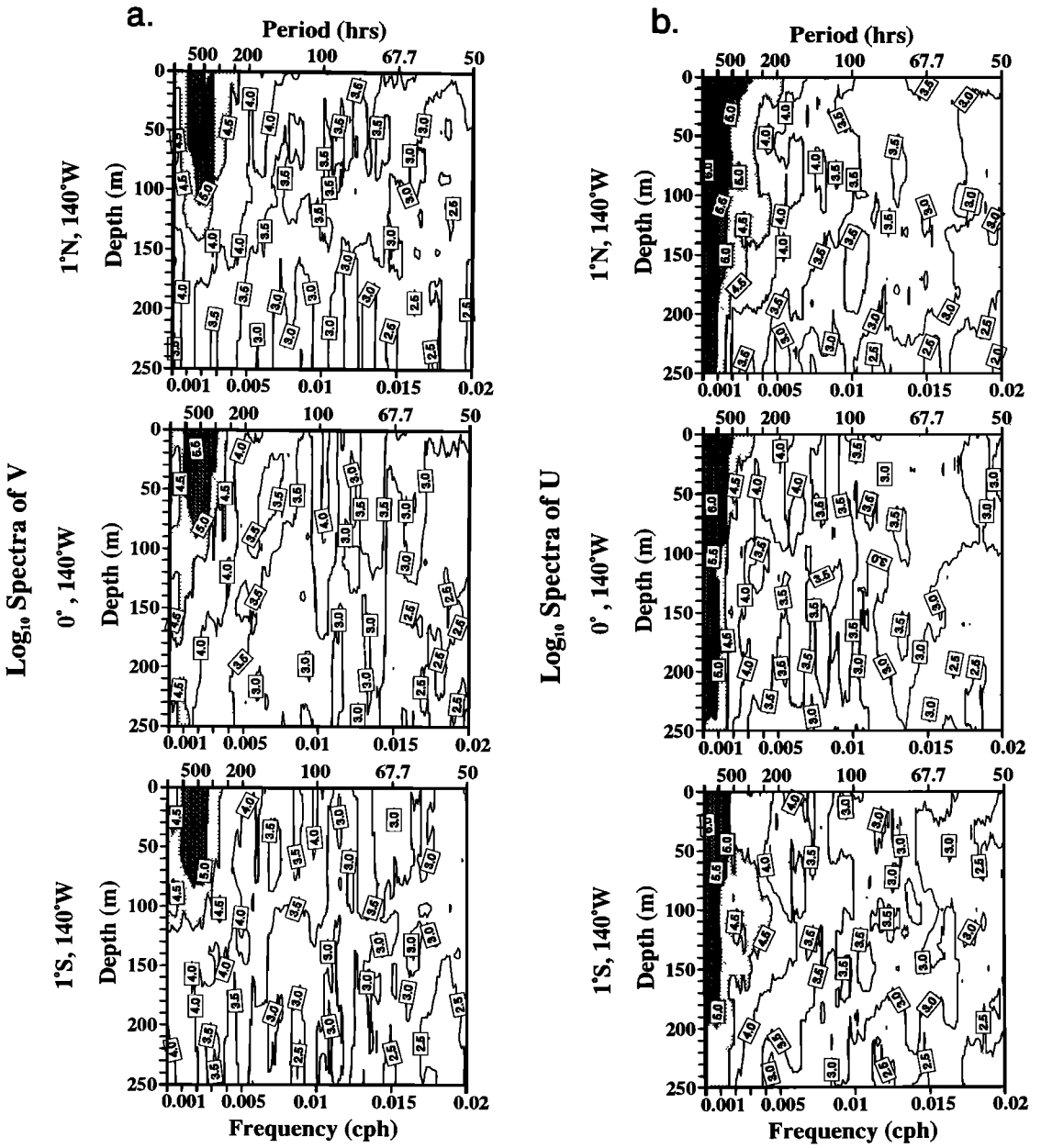

Figure 6. Log variance densities as functions of depth and frequency for the (a) v component and (b) u component along 140°W at 1°S, 0°, and 1°N. With a contour interval of 0.5 the lightly stippled areas highlight densities between $10^{4.5}$ and 10^5 (square centimeters per second per cycles per hour), and darkly stippled areas highlight densities greater than 10^5. The spectra were averaged over a bandwidth of 0.92×10^{-3} cph for approximately 18 degrees of freedom.

Oceans by *Weisberg et al.* [1979a, b] and *Halpern et al.* [1988], respectively.

Additional properties of the hodograph description are the orientation of the semimajor axis and the stability of this ellipse orientation [e.g., *Gonella*, 1972]. Stable ellipses are generally limited in the spectra to the bandwidth of the instability waves centered on 2.00×10^{-3} cph (500 hours periodicity). As an example, Figure 8 shows the velocity hodographs calculated at 30 m depth for each of the TIWE moorings, with the spectral bandwidth increased to essentially encompass all of the instability wave variance. On average, the near-surface instability wave oscillations consist of highly eccentric ellipses, oriented northward, but tilting toward the east, with this tilt increasing from nearly zero at 1°S to maximum values at 1°N. The direction of tilt, into the shear of the SEC (or equivalently into the shear between the SEC and the EUC at slightly deeper depths), is consistent with barotropic instability extracting perturbation wave energy from the mean flow. These tilts decrease with depth, and the ellipse stability becomes statistically insignificant by the EUC core depth. Thus, where stable, the hodographs provide kinematical support for the hypothesis of wave generation by barotropic instability. The hodographs further suggest that the maximum wave–mean flow interaction occurs within the cyclonic shear regions of the surface SEC and the border

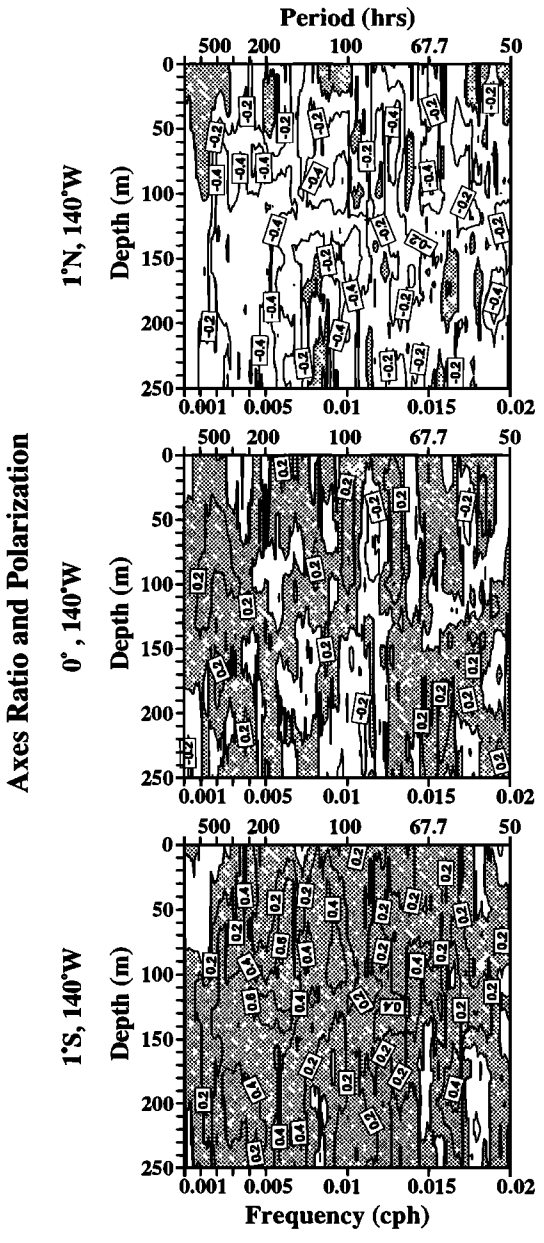

Figure 7. Semiminor to semimajor axes ratio for the velocity hodograph ellipse as a function of depth and frequency along 140°W at 1°S, 0°, and 1°N. Stippled and open regions denote anticlockwise and clockwise polarizations, respectively. The spectra were averaged over a bandwidth of 0.92 $\times 10^{-3}$ cph for approximately 18 degrees of freedom.

between the SEC and the EUC, consistent with the previous findings cited in section 2.

The narrowband nature of the instability waves suggests a complex demodulation analysis [e.g., *Bloomfield*, 1976] for examining the distribution of amplitude in time and space. This was performed over a 1.58 $\times 10^{-3}$ cph bandwidth centered upon 2.00 $\times 10^{-3}$ cph, as in the hodograph description. The analysis consists of Fourier transforming the time series, shifting the analysis bandwidth to be centered upon zero frequency, band-pass filtering the shifted Fourier transform to exclude all coefficients outside the analysis bandwidth, and then inverting the Fourier transform. The amplitude of the ensuing complex-valued time series gives the amplitude envelope of the fluctuations, and the rate of change of phase gives the deviation of the frequency from the central frequency. The amplitude results at 1°N, 0°, and 1°S along 140°W for v and u are shown in Figures 9 and 10, respectively. For the v component the amplitude shows the seasonality and the near-surface trapping of the instability waves. During the instability wave season the amplitude tends to be largest on the equator and at all locations it decreases rapidly below either surface maxima (or near-surface maxima at 1°N) to background levels at the EUC core. The amplitude begins to build in June 1990; several peaks are observed thereafter, with the maximum amplitude exceeding 60 cm s^{-1} on the equator.

The u component amplitude extends over a longer duration and depth range and is not as well organized as the v component. Larger u component amplitudes are also observed off the equator than on the equator, with the amplitudes being largest at 1°N. The elevated off-equator u component amplitudes at the EUC core depth may be a kinematical consequence of advection in the presence of the mean meridional shear on either side of the EUC. A cross-spectral analysis between $\partial u/\partial t$ and v at the off-equator locations (using the same bandwidth as in the hodograph analysis) shows high values of coherence squared (greater than 0.6) at and below the EUC core for periodicities between the instability waves and about 1 week. Where coherent, the phase switches from in phase north of the equator to π radians out of phase south of the equator, and the transfer function amplitude has magnitude consistent with the addition of the local mean meridional shear to the Coriolis parameter. By accounting for these deep, off-equator u component fluctuations kinematically, the similarities between the v and u component amplitudes (being largest north of the equator and near the surface) become consistent with a near-surface instability mechanism.

5. Wave Kinematics

With 115 time series of horizontal velocity vectors (5 locations × 23 depths) an efficient analysis technique is required to determine their interrelationships. Empirical orthogonal function (EOF) analysis [e.g., *Preisendorfer*, 1988] provides a data dependent way of separating the coherent wave signatures from the extraneous background fluctuations. EOF analysis transforms a set of time series into a set of orthogonal modes that span the data space, with each mode accounting for a successively smaller portion of the total data set variance. For a coherent array, most of the wave-related variance will reside within one mode, the structure of which describes the kinematical properties of the wave field. EOFs may be calculated in several ways: in the time domain using correlation or covariance matrices, in the frequency domain using coherence or cross-spectral matrices, or by Hilbert transform which is a hybrid between the time and frequency domain approaches. For wave analysis, wherein information on phase propagation is critical, analyses in the frequency domain or by Hilbert transform are the most useful. The present study used several of these approaches, including treating the v and the u components separately as well as together. The calculations found to be most useful were by frequency domain and Hilbert transform applied separately to the v components, since the v

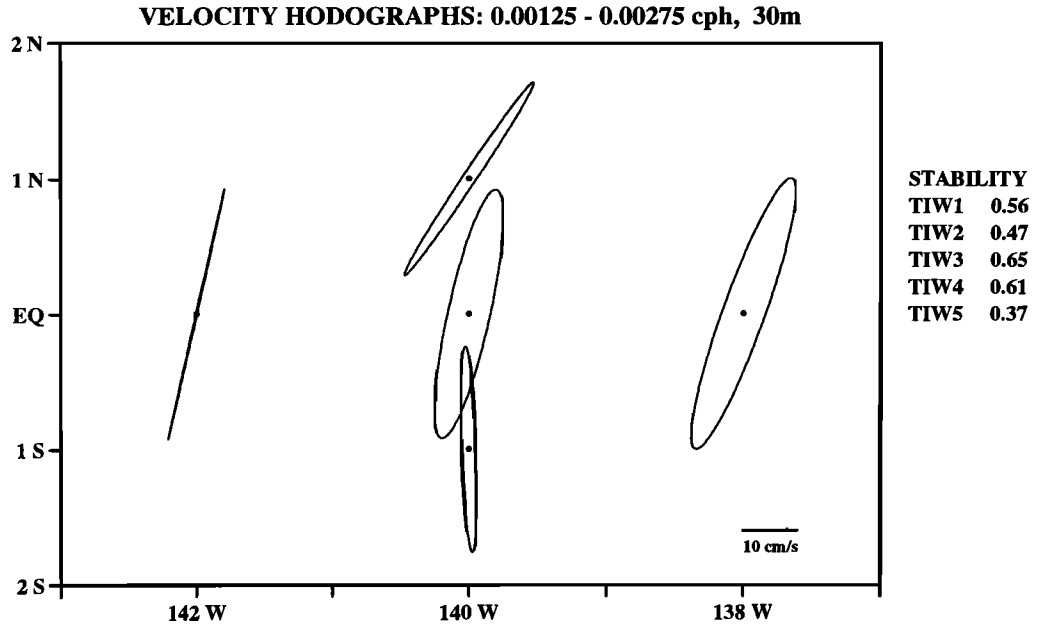

Figure 8. Velocity hodograph ellipses at 30 m depth at each of the five TIWE equatorial array mooring locations. The ellipses are from spectral averages over a 1.58×10^{-3} cph bandwidth centered on 2.00×10^{-3} cph with approximately 29 degrees of freedom. Ellipse stability is given on the right relative to a 90% significance level of 0.15.

components are the most coherent and energetic portion of the data set and they are not contaminated by the kinematical effects of background current shear advection.

The EOF analyses were thus performed on the v components from the five mooring locations, each with time series at 23 depths between 30 and 250 m. Extrapolated data above 30 m were omitted because they are not independent. The frequency domain analysis consisted of calculating the coherence (or cross spectral) matrices averaged with approximately 29 degrees of freedom (as in the velocity hodograph and the complex demodulation analyses), finding their eigenvalues and eigenvectors, projecting the Fourier transformed data onto the eigenvectors to get transfer functions for each mode (the principal components), and then determining the coherence between each mode and the data at each sample location. The Hilbert transform analysis employed the same bandwidth. The procedure was to band-pass filter and Hilbert transform the time series and then calculate the correlation (or covariance) matrices and their respective EOFs in the time domain. This results in a set of complex eigenvectors in space and principal components in time with similar information content as in the frequency domain EOF.

The first two modes of the frequency domain EOF using the coherence matrix accounted for 53% and 21% of the total normalized variance, respectively. These two modes are statistically separable following the criteria of *North et al.* [1982], and they are distinctly separate in space, with the first (second) mode primarily describing the variance distribution over the upper (lower) half of the sampled water column. The first-mode results given in Figure 11 are therefore used to describe the instability waves. Shown are the mode amplitude as a function of depth at each of the mooring locations (Figure 11a), the coherence squared between this mode and the data as a function of depth at each of the mooring locations (Figure 11b), the phase distribution as a function of longitude and depth along the equator (Figure 11c), and the phase distribution as a function of latitude and depth along 140°W (Figure 11d). The amplitudes are largest on the equator (note that these are rms values, as opposed to time varying amplitudes in the complex demodulation). At all but the 1°N location the amplitudes drop precipitously from their near-surface maxima, reaching background levels by 130 m. The amplitudes at 1°N also drop precipitously with depth, but below a maximum at 50–80 m. The coherence distributions generally show largest values over the region where the amplitudes are above the background levels. Thus, above the EUC core, where the instability wave oscillations are most readily observed, some 80% of the v component variance is accounted for by this first EOF mode.

The zonal and meridional slices through the first-mode phase space provide phase propagation information. Where the mode and the data are coherent, these phases have relatively narrow error bars (given in the appendix). Above 100 m the 90% confidence intervals are smaller than ± 0.2 rad which is much smaller than the zonal phase differences. These intervals increase with depth, but they remain smaller than the zonal phase differences along equator. To the contrary, the vertical and meridional phase differences are smaller than the 90% confidence intervals at all locations.

The zonal phase distribution along the equator shows a very uniform phase gradient above 90 m. Here the direction of phase propagation is westward and downward. Below 90 m the zonal direction persists, while the vertical direction changes to upward and then downward again. In all cases the vertical phase differences are small and not statistically different from zero; however, it is curious that the changes in the sense of vertical phase propagation coincide with the upper and the lower portions of the thermocline within which the EUC is located. The meridional phase distribution along 140°W is not as well defined as the zonal phase

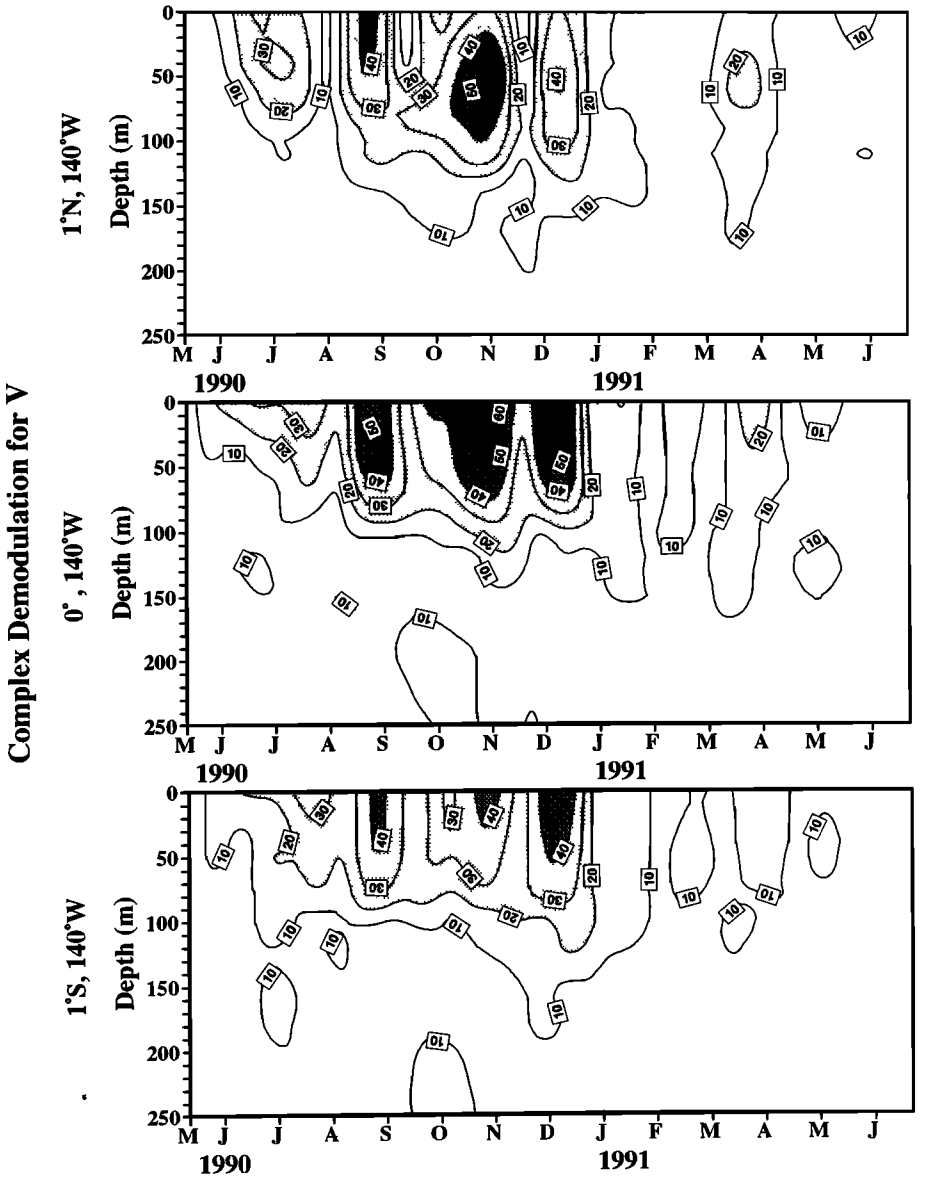

Figure 9. The complex demodulation amplitude for the v component as a function of depth and time along 140°W at 1°S, 0°, and 1°N computed over a 1.58×10^{-3} cph bandwidth centered on 2.00×10^{-3} cph. Stippling highlights regions with amplitudes greater than 20 cm s^{-1}.

distribution along the equator. Above the thermocline the meridional component of the phase gradient is small and statistically indeterminate. The largest meridional phase gradient region lies between the equator and 1°N at the EUC core depth, but again this is not statistically different from zero. In summary, the phase distributions show very well defined zonal propagation, essentially no meridional propagation, and interesting, but statistically insignificant, vertical propagation.

With the spatial variations in phase statistically significant at least in the zonal direction, estimates of horizontal wavenumber vectors were made by independently fitting planes to the phase information at each depth using linear least squares regression. The implied assumption is that the zonal and meridional wavenumber components at each depth are uniform over the array; deviations from this assumption result in error. Since none of the vertical phase differences are statistically significant, similar analyses in the vertical were not performed. The procedure is as follows. At any specified depth, let ϕ_i be the EOF phase at the ith sample location (x_i, y_i). A horizontal plane fit of the form $\varphi_0 + kx + ly + \varphi_0$ [(k, l) being the wavenumber vector components in (x, y)) is sought to ϕ_i in a manner that minimizes the sum of the squares of the errors:

$$D^2 = \sum_{i=1}^{5} [\phi_i - (kx_i + ly_i + \varphi_0)]^2$$

Figure 12 shows the resulting k, l as a function of depth, along with the 90% confidence intervals for random errors (an error analysis including the EOF and linear regression

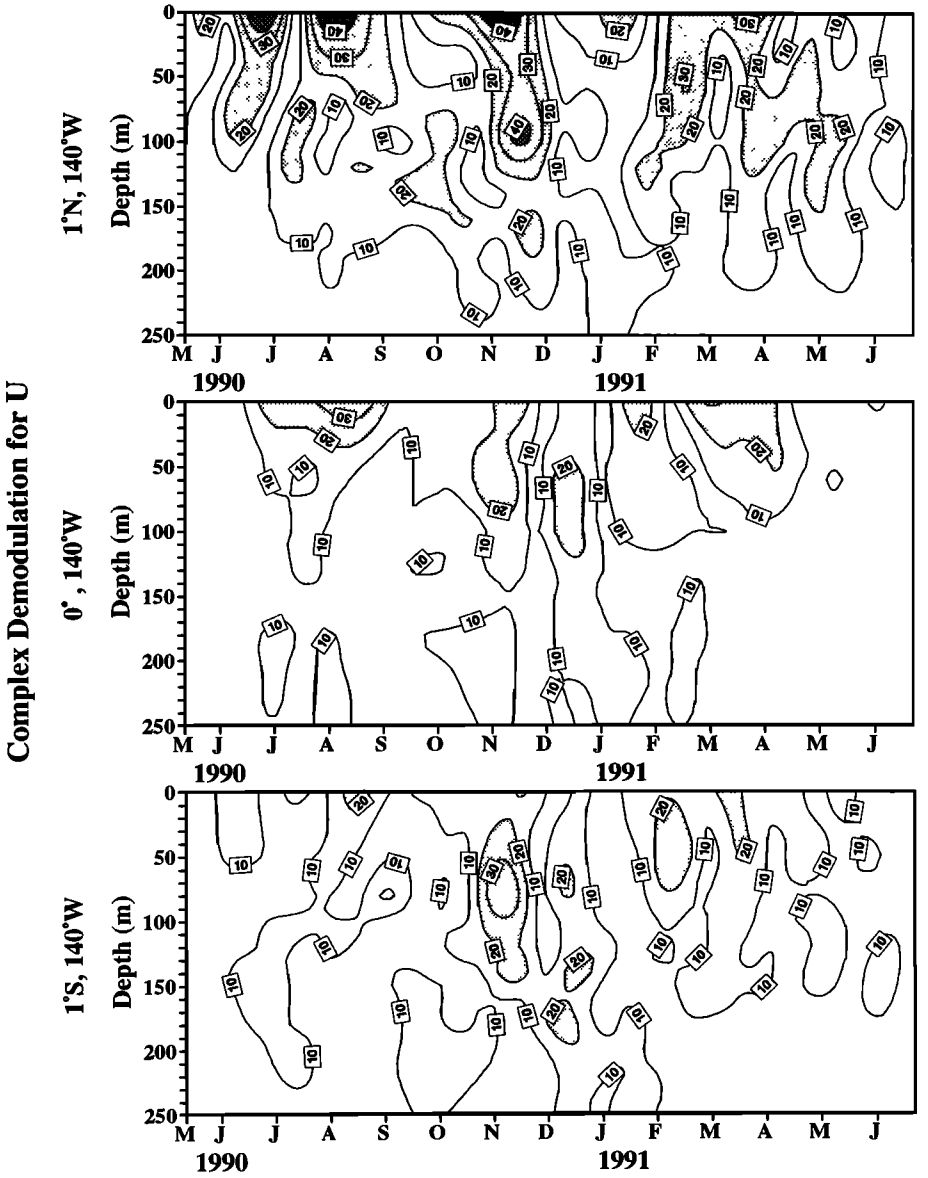

Figure 10. The complex demodulation amplitude for the u component as a function of depth and time along 140°W at 1°S, 0°, and 1°N computed over a 1.58×10^{-3} cph bandwidth centered on 2.00×10^{-3} cph. Stippling highlights regions with amplitudes greater than 20 cm s^{-1}.

contributions is given in the appendix). The results for the zonal wavenumber component are uniform and with small error bars over the upper 110 m. Within this region, k is directed westward, with magnitude 5.9×10^{-3} km^{-1} and confidence interval less than $\pm 1.1 \times 10^{-3}$ km^{-1}, corresponding to a wavelength and wavelength range of 1060 km and between 900 and 1300 km. Below 110 m, k begins to vary and the error bars increase, but the direction remains westward within the 90% confidence interval. In contrast to k, the meridional wavenumber component l, while showing a small northward directed mean, is not statistically different from zero at any of the observed depths.

Repeating the analysis using the cross-spectral matrix shows nearly identical results. Since the cross-spectral matrix is weighted by the actual distribution of variance, it follows that the region above the thermocline influences the first mode the most, resulting in 82% of the total variance being contained in this mode, with phase estimates having slightly smaller (larger) error above (below) 110 m. The spatial information from the Hilbert transform analysis was also the same. Additional information (not shown) pertains to the amplitude and frequency modulation of the fluctuations within the analyzed bandwidth. Paralleling a complex demodulation, the amplitude and the rate of change of phase for the first mode give the amplitude and the frequency modulations, respectively, for the time variations of that mode. An advantage over complex demodulation is that, presumably, the Hilbert transform EOF separates coherent wave motions from incoherent variability. The amplitude modulation results were similar to those found for the individual time series, and the frequency modulation showed small variations about 2.0×10^{-3} cph, consistent with a

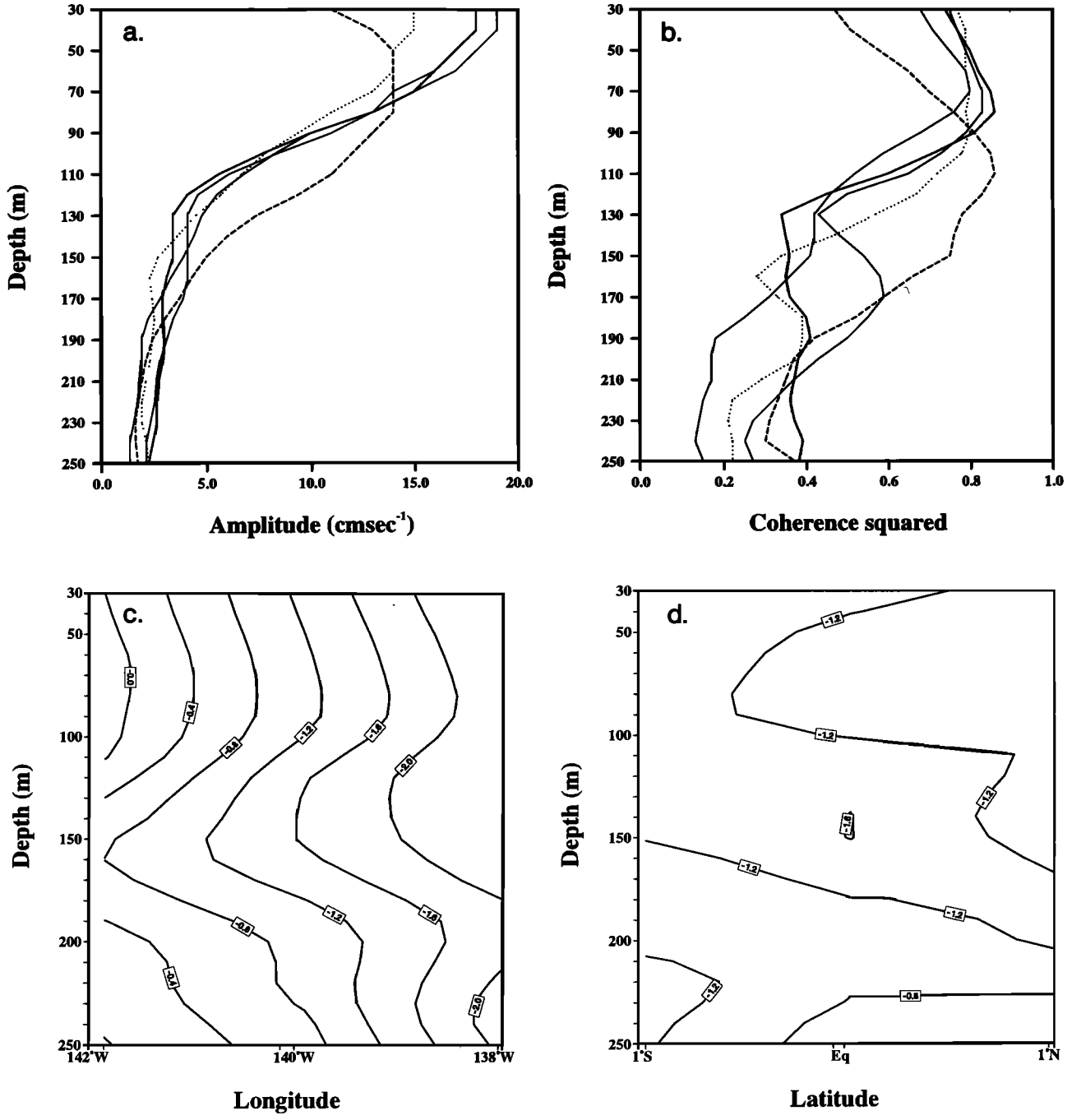

Figure 11. The first (frequency domain) empirical orthogonal function (EOF) mode for the v component calculated from the coherence matrix averaged over a 1.58×10^{-3} cph bandwidth centered on 2.00×10^{-3} cph (approximately 29 degrees of freedom). (a) Amplitudes as a function of depth at each mooring location (solid lines for the equator locations, dashed line for 1°N, and dotted line for 1°S). (b) Coherence squared between the first mode and the data as a function of depth at each mooring location (90% significance level = 0.15, and the line designations are the same as Figure 11a). (c) Phase (radians) as a function of longitude and depth along the equator. (d) Phase (radians) as a function of latitude and depth along 140°W. The contour interval on the phase maps is 0.4 rad, and phase has been interpolated to account for the moorings not being precisely on the equator or on 140°W. The 90% confidence interval (see appendix) is less than 0.2 rad above 100 m and greater than 1.0 rad below 180 m.

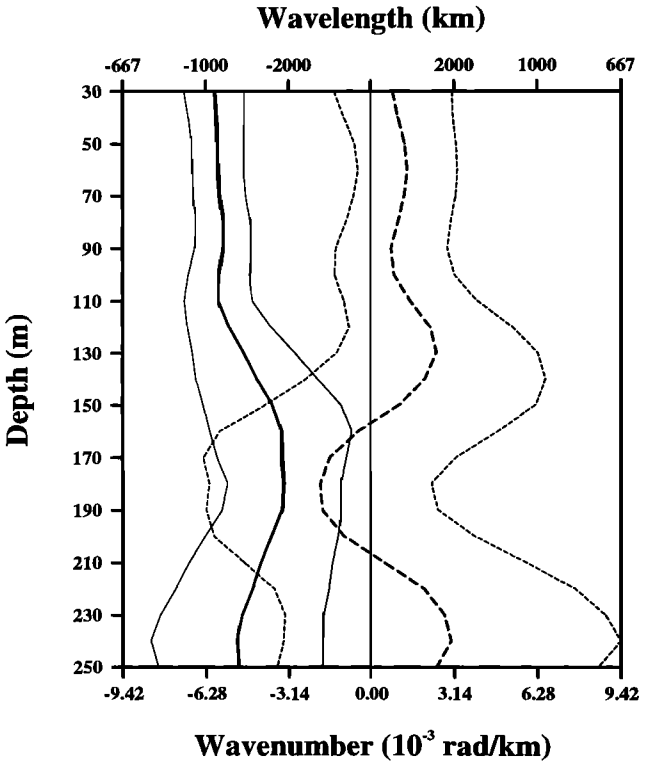

Figure 12. The zonal (solid lines) and meridional (dashed lines) wavenumber vector components as a function of depth, along with their 90% confidence intervals for random errors (see appendix) calculated at 0°, 140°W using the v component first EOF mode and independent plane fits by linear regression at each depth.

periodogram analysis performed in choosing the analysis bandwidth. The main findings of this section are therefore independent of the various analysis techniques employed.

6. Discussion and Summary

High vertical resolution profiles of horizontal velocity vectors obtained from an equatorial Pacific array of subsurface moored ADCPs were used to examine the kinematics of tropical instability waves observed during 1990. The distribution of variance showed a well-defined wave season lasting from August to December, with wave variance confined primarily to the near-surface region above the EUC core. The onset of the wave season coincided with the acceleration of the SEC, and the termination coincided with a strong eastward momentum pulse propagating from the west as a Kelvin wave. The instability wave velocity fluctuations may be described by highly eccentric ellipses, oriented to the north, but tilting toward the east into the cyclonic shear of the SEC. Over the observational domain (1°S to 1°N and 142°W to 138°W) these tilts increased with latitude from essentially zero at 1°S to maximum values at 1°N and decreased with depth from maximum values at the uppermost 30-m measurement. By the EUC core at 110 m the wave variances, hodograph tilts, and ellipse stabilities were all nil.

The instability wave variance was contained within a narrow frequency band centered upon 500-hour periodicity. Averaged over this bandwidth, the zonal wavenumber component was uniform, with depth between 30 and 110 m and directed westward with a magnitude and 90% confidence interval of $5.9 \times 10^{-3} \pm 1.1 \times 10^{-3}$ rad km^{-1} (or a wavelength of 1060 km and a 90% confidence interval between 900 and 1300 km). The corresponding westward directed phase speed was 59 cm s^{-1}. Unlike the zonal component, neither the meridional nor the vertical wavenumber component was statistically different from zero.

The systematic tilting of the velocity hodographs is consistent with previous findings of wave generation by barotropic instability within the near-surface cyclonic shear region north of the equator. With the instability waves' onset tied to the acceleration of the SEC and the waves' kinetic energy confined primarily above the thermocline and hence above the EUC core, wave generation appears to be associated with the westward flowing SEC. However, the cyclonic shear of the SEC is related to the eastward flowing EUC, which has led some authors [e.g., *Lukas*, 1987; *Wilson and Leetmaa*, 1988; *Luther and Johnson*, 1990] to argue for generation within the EUC/SEC shear region. From the hodograph tilts the Reynolds stresses are largest nearest the surface, but the background shear is largest below the surface. Since the Reynolds stresses and the background shear both enter into the mean flow to wave energy conversion, it is difficult to label the specific current in which this occurs. The SEC appears to go unstable, but this would not occur if the entire flow field did not have the necessary meridional shear and curvature that the EUC, along with hemispherically asymmetric wind stress, provides. The eastward momentum the EUC sharpens the positive curvature at the westward flowing SEC maximum north of the equator and causes cyclonic shear equatorward of this maximum. Owing to β, the positive curvature of the SEC may be destabilizing while the negative curvature of the EUC is stabilizing, with divergence further tending to destabilize the SEC [e.g., *Philander*, 1976]. The hemispheric asymmetry in wind stress also accentuates the northern maximum, increasing the magnitude of the cyclonic shear north of the equator and maintaining the sign of the shear across the equator (for symmetric winds the shear would be zero on the equator). The resultant near-surface current profiles given for the Pacific and Atlantic Oceans by *Hansen and Paul* [1984] and *Richardson and McKee* [1984], respectively, thus show maximum positive curvature at about 2°–3°N and negative (cyclonic north of the equator) shear from that point across the equator. From these findings, along with the *Philander* [1978] $1\frac{1}{2}$-layer stability analysis that utilized a realistic surface current distribution without a subsurface EUC, it may be hypothesized that the eastward EUC provides a catalyst for instability (by shaping the SEC) while itself being inherently stable.

The period and zonal wavelength estimates are consistent with previous results (Table 1), even including the earliest short duration, statistically indeterminate estimates from the GATE program. This provides an example in geophysics where the results from an ensemble of independent measurements may be compared within confidence intervals inferred by an ergodic hypothesis, and the comparison is very good. It may be concluded that the instability waves derive from a seasonally modulated, but stationary, random process that is narrowband in frequency and zonal wavenumber. Barotropic instability as a mechanism for wave generation is qualitatively understood, but the selection of the central fre-

quency and wavenumber, along with additional mechanisms of instability, requires more theoretical guidance.

Appendix

A1. Error Analysis for Phase

Consider the linear relationship between the input and output time series $x(t)$ and $y(t)$ with spectral estimates $G_x(f)$ and $G_y(f)$, respectively, and transfer function $H(f)$ [e.g., *Bendat and Piersol*, 1971]. The phase of the transfer function is:

$$\phi = \tan^{-1} \frac{\text{Im}\,[H(f)]}{\text{Re}\,[H(f)]} \tag{A1}$$

and the confidence interval for random errors is estimated by

$$\Delta\phi = \sin^{-1} \frac{r(f)}{|H(f)|} \tag{A2}$$

where

$$r^2(f) = \frac{2}{n-2} F_{2,n-2;\alpha}(1 - \gamma_{xy}^2) \frac{G_x(f)}{G_y(f)}$$

n is the number of degrees of freedom for the spectral estimates, $F_{2,n-2;\alpha}$ is the 100α percentage point for the F distribution with 2 and $n-2$ degrees of freedom, and $\gamma_{xy}^2(f)$ is the estimated coherence squared between $x(t)$ and $y(t)$.

Using the first EOF mode as input and the data at a given location as output, the relative phases and the confidence intervals between the mode and the data are estimated using (A1) and (A2). Figures A1a and A1b shows the resulting 90% confidence intervals for the phase determinations in the zonal and meridional planes of Figures 11c and 11d, respectively.

A2. Error Analysis for Wavenumber

The horizontal components of the wavenumber vector are estimated by fitting planes independently at each depth between 30 and 250 m to the five phase estimates using linear least squares regression. The basic assumption of the linear regression is that wavenumber vector is constant over the array. Deviations from this assumption lead to imperfect fit and, consequently, to error. The following outlines the error analyses.

Denote the wavenumber vector as (k, l), the EOF mode phases at each of the five locations as $\phi_i (i = 1, \ldots, 5)$, and the phase function to be fit by linear regression as $\varphi_i = kx + ly + \varphi_0 (i = 1, \ldots, 5)$. Each of the ϕ_i computed by the EOF analysis has n degrees of freedom (29 in this case). Statistically, this is equivalent to expressing ϕ_i as the average over n measurements $\phi_{i,j}$, $(j = 1, \ldots, n)$.

$$\phi_i = \frac{\sum_{j=1}^{n} \phi_{i,j}}{n} \qquad i = 1, \ldots, 5$$

The linear least squares regression minimizes the sum of the squares of the deviations between the phases ϕ_i and the phase function φ_i to be fit, i.e.,

$$\sum_{i=1}^{5} (\phi_i - \varphi_i)^2.$$

This results in a set of linear equations for (k, l) given by

$$\begin{pmatrix} k \\ l \end{pmatrix} = \begin{pmatrix} c_{11} c_{12} \\ c_{21} c_{22} \end{pmatrix} \begin{pmatrix} b_1 \\ b_2 \end{pmatrix} \tag{A3}$$

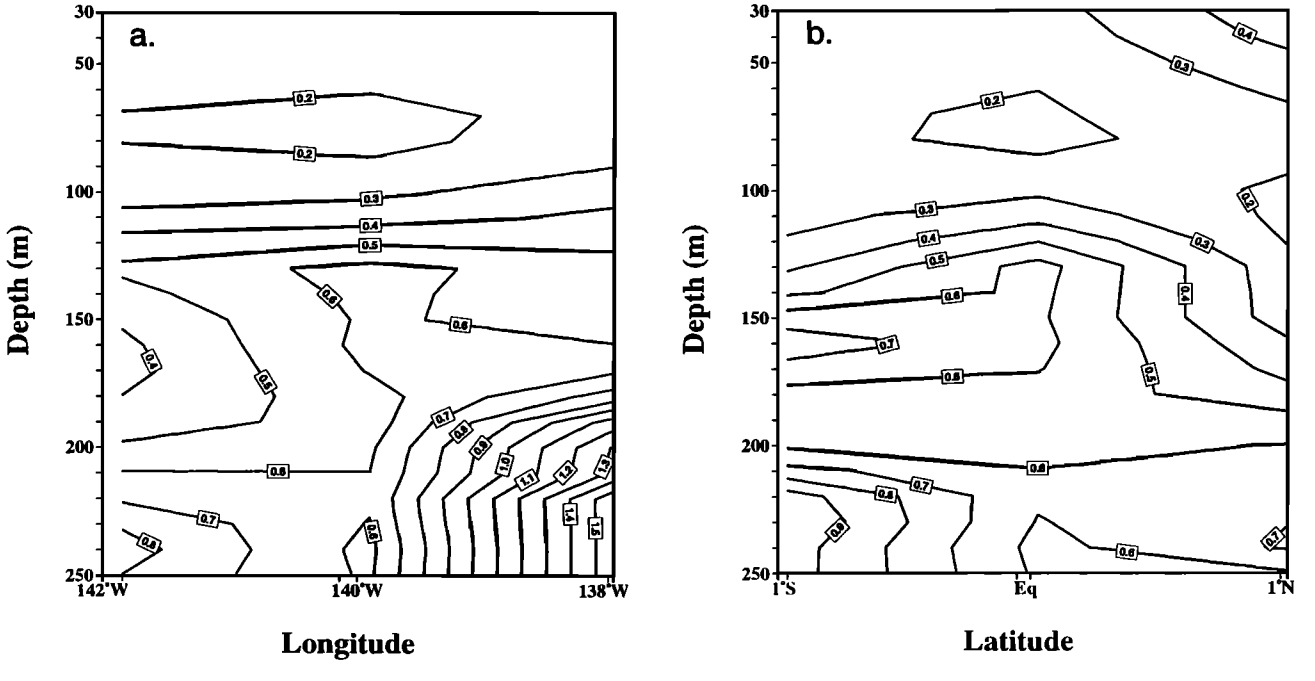

Figure A1. The 90% confidence intervals for random errors on phase (a) as a function of longitude and depth along 140° and (b) as a function of latitude and depth along the equator for comparison with the phase estimations of Figures 11c and 11d, respectively. The contour interval is 0.1 rad.

where

$$C = \begin{pmatrix} c_{11} c_{12} \\ c_{21} c_{22} \end{pmatrix} = \begin{pmatrix} a_{11} a_{12} \\ a_{21} a_{22} \end{pmatrix}^{-1}$$

$$a_{11} = \tfrac{1}{5} \sum_{i=1}^{5} x_i^2 - \tfrac{1}{5} \left(\sum_{i=1}^{5} x_i \right)^2$$

$$a_{12} = a_{21} = \tfrac{1}{5} \sum_{i=1}^{5} x_i y_i - \tfrac{1}{25} \left(\sum_{i=1}^{5} x_i \right) \left(\sum_{i=1}^{5} y_i \right)$$

$$a_{22} = \tfrac{1}{5} \sum_{i=1}^{5} y_i^2 - \tfrac{1}{25} \left(\sum_{i=1}^{5} y_i \right)^2$$

$$b_1 = \tfrac{1}{5} \sum_{i=1}^{5} \phi_i x_i - \tfrac{1}{25} \left(\sum_{i=1}^{5} \phi_i \right) \left(\sum_{i=1}^{5} x_i \right)$$

$$b_2 = \tfrac{1}{5} \sum_{i=1}^{5} \phi_i y_i - \tfrac{1}{25} \left(\sum_{i=1}^{5} \phi_i \right) \left(\sum_{i=1}^{5} y_i \right)$$

and (x_i, y_i) is the ith station location.

The total number of degrees of freedom includes the degrees of freedom for each of the original phase estimates combined with the additional number of degrees of freedom associated with the plane fits to these estimates. At each depth there are five phase estimates; however, the plane fit has three constraints: k, l, and φ_0. Therefore the linear regression used to estimate the wavenumber vector increases the number of degrees of freedom by a factor of 2, rather than 5. The number of degrees of freedom for the (k, l) determination is thus $(5 - 3)n$, or 58. This is sufficiently large so that the probability distribution function for k and l may be approximated by a student's-t distribution regardless of their true distribution. Given the student's-t distribution, the errors for (k, l) may be expressed as

$$\begin{pmatrix} \Delta k \\ \Delta l \end{pmatrix} = t(1 - \alpha, 58)\ \mathrm{SD} \begin{pmatrix} c_{11} \\ c_{22} \end{pmatrix} \tag{A4}$$

where $t(1 - \alpha, 58)$ is the student's-t distribution at the $(1 - \alpha)\%$ confidence level with 58 degrees of freedom and SD is the standard deviation of the phase φ to be determined.

By definition, SD follows from

$$\mathrm{SD}^2 = \frac{1}{(5-3)n} \sum_{i=1}^{5} \left[\sum_{j=1}^{n} (\phi_{i,j} - \varphi_i)^2 \right]$$

$$= \frac{1}{2n} \sum_{i=1}^{5} \left[\sum_{j=1}^{n} (\phi_{i,j} - \phi_i + \phi_i - \varphi_i)^2 \right]$$

$$= \frac{1}{2n} \sum_{i=1}^{5} \left[\sum_{j=1}^{n} (\phi_{i,j} - \phi_i)^2 + (\phi_i - \varphi_i)^2 + 2(\phi_{i,j} - \phi_i)(\phi_i - \varphi_i) \right]$$

$$= \frac{1}{2n} \sum_{i=1}^{5} \left[n(\phi_i - \varphi_i)^2 + \sum_{j=1}^{n} (\phi_{i,j} - \varphi_i)^2 \right] \tag{A5}$$

where it has been assumed that $\phi_i - \varphi_i$ and $\phi_{i,j} - \phi_i$, the errors from linear regression and EOF analyses, respectively, are uncorrelated. This is a reasonable assumption, since these two calculation are performed independently. The first part of error in (A5), the deviations from the plane fit, is straightforward. The second part of the error requires an evaluation of (A2), which is the variance of the phase ϕ_i obtained by linear systems analysis. By definition

$$\frac{1}{n} \sum_{j=1}^{n} (\phi_{i,j} - \phi_i)^2 = \mathrm{Var}\ \{\phi_i\}$$

$$= \mathrm{E}\{\Delta\phi^2\}$$

$$= \int_{\pi/2}^{\pi/2} \Delta\phi^2 p(\Delta\phi)\ d\Delta\phi \tag{A6}$$

where $p(\Delta\phi)$ is the unknown probability density function for $\Delta\phi$. While $p(\Delta\phi)$ is unknown, an upper bound may be estimated by noting that for the interval $(\pi/2) \le \Delta\phi \le (\pi/2)$, $|\sin\Delta\phi| \ge |(2/\pi)\ \Delta\phi|$. Using this in (A6), along with (A2), results in

$$\int_{\pi/2}^{\pi/2} \Delta\phi^2 p(\Delta\phi)\ d\Delta\phi \le \int_{\pi/2}^{\pi/2} \left(\frac{\pi}{2} \right)^2 \sin^2 \Delta\phi p(\Delta\phi)\ d\Delta\phi$$

$$= \frac{\pi^2}{4} \mathrm{E}\left\{ \left[\frac{r(f)}{H(f)} \right]^2 \right\}$$

Thus, we can use $\mathrm{E}\{[r(f)/H(f)]^2\}$ at each location as an upper bound on the variance of ϕ_i. Evaluating the expectation operation by assuming that the F distribution is uncorrelated with the observed spectra gives

$$\mathrm{E}\left\{ \left[\frac{r(f)}{H(f)} \right]^2 \right\} = \frac{2}{n-2} \mathrm{E}(F_{2,n-2;\alpha}) \cdot \mathrm{E}\left[(1 - \gamma_{xy}^2) \frac{G_y(f)}{H(f) G_x(f)} \right]$$

$$= \frac{2}{n-2} \frac{n-2}{n-4} \frac{(1 - \gamma_{xy}^2)}{\gamma_{xy}^2}$$

$$= \frac{2}{n-4} \frac{(1 - \gamma_{xy}^2)}{\gamma_{xy}^2}$$

from which we may now estimate SD by:

$$\mathrm{SD}^2 = \tfrac{1}{2} \sum_{i=1}^{5} (\phi_i - \varphi_i)^2 + \frac{\pi^2}{4n(n-4)} \sum_{i=1}^{5} \left(\frac{1 - \gamma_{xy}^2}{\gamma_{xy}^2} \right)_i \tag{A7}$$

In summary, errors for (k, l) are estimated using (A4), with SD calculated from (A7). The first part is due to nonuniformity in the wavenumber vector over the array and hence an imperfect plane fit. The second part is due to the variance of the EOF phase. The latter forms the larger

portion of the error above 110 m, and below 140 m both sources of error are comparable and larger than their values above 110 m. Thus, where the EOF mode best fits the data (above 110 m), the horizontal wavenumber vector is very uniform over the array.

Acknowledgments. Support was provided by the Ocean Sciences Division, National Science Foundation, grants OCE-8813378 and OCE-9302811. R. Cole and J. Donovan assisted with the field work and analyses, and sea going operations were facilitated by the officers and crew of the R/V *Wecoma* and *Alpha Helix*.

References

Bendat, J. S., and A. G. Piersol, *Random Data: Analysis and Measurement Procedure*, Wiley-Interscience, New York, 1971.

Bloomfield, P., *Fourier Analysis of Time Series: An Introduction*, John Wiley, New York, 1976.

Brown, O. B., Observation of long period sea surface temperature variability during GATE, *Deep Sea Res., Part A, 26*, suppl. 2, 103–124, 1979.

Bryden, H. L., and E. C. Brady, Eddy momentum and heat fluxes and their effects on the circulation of the equatorial Pacific Ocean, *J. Mar. Res., 47*, 55–79, 1989.

Charney, J., and P. G. Drazin, Propagation of planetary-scale disturbances from the lower into the upper atmosphere, *J. Geophys. Res., 66*, 83–109, 1961.

Cox, M., Generation and propagation of 30-day waves in a numerical model of the Pacific, *J. Phys. Oceanogr., 10*, 1168–1186, 1980.

Düing, W., et al., Meanders and long waves in the equatorial Atlantic, *Nature, 235*, 280–284, 1975.

Eliassen, A., and E. Palm, On the transfer of energy in stationary mountain waves, *Geophys. Norv., 22*, 1–23, 1960.

Eriksen, C. C., and J. G. Richman, An estimate of equatorial wave energy flux at 9- to 90-day periods in the central Pacific, *J. Geophys. Res., 93*, 15,455–15,466, 1988.

Gonella, J., A rotary component method for analysing meteorological and oceanographic vector time series, *Deep Sea Res., 19*, 833–846, 1972.

Halpern, D., Detection of 17.5-day period meridional current oscillations in the Equatorial Western Pacific Ocean during 1985, *Geophys. Res. Lett., 16*, 499–502, 1989.

Halpern, D., and R. H. Weisberg, Upper ocean thermal and flow fields at 0°, 28°W (Atlantic) and 0°, 140°W (Pacific) during 1983–1985, *Deep Sea Res., Part A, 39*, 407–418, 1989.

Halpern, D., S. P. Hayes, A. Leetmaa, D. Hansen, and S. G. H. Philander, Oceanographic observations of the 1982 warming of tropical eastern Pacific, *Science, 221*, 1173–1175, 1983.

Halpern, D., R. A. Knox, and D. S. Luther, Observations of 20-day period meridional current oscillations in the upper ocean along the Pacific equator, *J. Phys. Oceanogr., 18*, 1514–1534, 1988.

Hansen, D., and C. Paul, Genesis and effects of long waves in the equatorial Pacific, *J. Geophys. Res., 89*, 10,431–10,440, 1984.

Harvey, R. R., and W. C. Patzert, Deep current measurements suggest long waves in the eastern equatorial Pacific, *Science, 193*, 883–884, 1976.

Johns, W. E., Near-surface current measurements in Gulf Stream using an upward-looking acoustic Doppler current profiler, *J. Atmos. Oceanic Technol., 5*, 602–613, 1988.

Legeckis, R., Long waves in the eastern Equatorial Pacific Ocean: A view from a geostationary satellite, *Science, 197*, 1179–1181, 1977.

Legeckis, R., Long waves in the equatorial Pacific and Atlantic Oceans during 1983, *Ocean Air Inter., 1*, 1–10, 1986.

Legeckis, R., and G. Reverdin, Long waves in the equatorial Atlantic Ocean during 1983, *J. Geophys. Res., 92*, 2835–2842, 1987.

Legeckis, R., W. Pichel, and G. Nesterczuk, Equatorial long waves in geostationary satellite observations and in a multichannel sea surface temperature analysis, *Bull. Am. Meteorol. Soc., 64*, 133–139, 1983.

Lukas, R., Horizontal Reynolds stresses in the central equatorial Pacific, *J. Geophys. Res., 92*, 9453–9463, 1987.

Luther, D. S., and E. S. Johnson, Eddy energetics in the upper equatorial Pacific during the Hawaii-to-Tahiti shuttle experiment, *J. Phys. Oceanogr., 20*, 913–944, 1990.

Luyten, J. R., and D. H. Roemmich, Equatorial currents at semiannual period in the Indian Ocean, *J. Phys. Oceanogr., 12*, 406–413, 1982.

Malardé, J.-P., P. D. Mey, C. Périgaud, and J.-F. Minster, Observation of long equatorial waves in the Pacific Ocean by Seasat altimetry, *J. Phys. Oceanogr., 17*, 2273–2279, 1987.

Mayer, D. A., R. L. Molinari, and R. H. Weisberg, Analysis of volunteer observing ship temperature fields in the tropical Atlantic Ocean, *Oceanol. Acta, 13*, 257–264, 1990.

McCreary, J. P., and Z. Yu, Equatorial dynamics in a 2 1/2-layer model, *Prog. Oceanogr., 29*, 61–132, 1992.

McPhaden, M. J., and B. A. Taft, Dynamics of seasonal and intraseasonal variability in the eastern equatorial Pacific, *J. Phys. Oceanogr., 18*, 1713–1732, 1988.

McPhaden, M. J., H. B. Milburn, A. I. Nakamura, and A. J. Shepard, PROTEUS: Profile Telemetry of Upper Ocean Currents, *Sea Technol., 32*, 10–19, February 1991.

Meyers, G., Annual variation in the slope of the 14°C isotherm along the equator in the Pacific Ocean, *J. Phys. Oceanogr., 9*, 885–891, 1979.

Miller, L., D. R. Watts, and M. Wimbush, Oscillations of dynamic topography in the eastern equatorial Pacific, *J. Phys. Oceanogr., 15*, 1759–1770, 1985.

Mitchell, T. P., and J. M. Wallace, The annual cycle in equatorial convection and sea surface temperature, *J. Clim., 5*, 1140–1156, 1992.

Mitchum, G. T., and R. Lukas, The latitude-frequency structure of Pacific sea level variance, *J. Phys. Oceanogr., 17*, 2362–2365, 1987.

Musman, S., Sea height wave form in equatorial waves and its interpretation, *J. Geophys. Res., 94*, 3303–3309, 1989.

North, G. R., T. L. Bell, R. F. Cahalan, and F. J. Moeng, Sampling errors in the estimation of Empirical Orthogonal Functions, *Mon. Weather Rev., 110*, 699–706, 1982.

Périgaud, C., Sea level oscillations observed with Geosat along the two shear fronts of the Pacific North Equatorial Countercurrent, *J. Geophys. Res., 95*, 7239–7248, 1990.

Philander, G., D. Halpern, D. Hansen, R. Legeckis, L. Miller, C. Paul, R. Watts, R. Weisberg, and M. Wimbush, Long waves in the equatorial Pacific Ocean. *Eos Trans. AGU, 66*, 154–155, 1985.

Philander, S. G. H., Instabilities of zonal equatorial currents, *J. Geophys. Res., 81*, 3725–3735, 1976.

Philander, S. G. H., Instabilities of zonal equatorial currents, 2, *J. Geophys. Res., 83*, 3679–3682, 1978.

Philander, S. G. H., W. J. Hurlin, and R. C. Pacanowski, Properties of long equatorial waves in models of the seasonal cycle in tropical Atlantic and Pacific Oceans, *J. Geophys. Res., 91*, 14,207–14,211, 1986.

Preisendorfer, R. W., *Principal Component Analysis in Meteorology and Oceanography*, Elsevier, New York, 1988.

Pullen, P., R. L. Bernstein, and D. Halpern, Equatorial long-wave characteristics determined from satellite sea surface temperature and in situ data, *J. Geophys. Res., 92*, 742–748, 1987.

Reverdin, G., and M. J. McPhaden, Near-surface current and temperature variability observed in equatorial Atlantic from drifting buoys, *J. Geophys. Res., 91*, 6569–6581, 1986.

Richardson, P. L., and T. K. McKee, Average seasonal variations of the Atlantic equatorial currents from historical ship drifts, *J. Phys. Oceanogr., 14*, 1226–1238, 1984.

Steger, J. M., and J. A. Carton, Long waves and eddies in the tropical Atlantic Ocean: 1984–1990, *J. Geophys. Res., 96*, 15,161–15,171, 1991.

Weingartner, T. J., and R. H. Weisberg, A description of the annual cycle in sea surface temperature and upper ocean heat in the Equatorial Atlantic, *J. Phys. Oceanogr., 21*, 83–96, 1991.

Weisberg, R. H., Equatorial waves during GATE and their relation to the mean zonal circulation, *Deep Sea Res., Part A, 26*, suppl. 2, 179–198, 1979.

Weisberg, R. H., Instability waves observed on the equator in the Atlantic Ocean during 1983, *Geophys. Res. Lett., 11*, 754–756, 1984.

Weisberg, R. H., and A. M. Horigan, Low-frequency variability in the equatorial Atlantic, *J. Phys. Oceanogr., 11*, 913–920, 1981.

Weisberg, R. H., and T. J. Weingartner, Instability waves in the

equatorial Atlantic Ocean, *J. Phys. Oceanogr.*, *18*, 1641–1657, 1988.

Weisberg, R. H., L. Miller, A. Horigan, and J. A. Knauss, Velocity observations in the equatorial thermocline during GATE, *Deep Sea Res., Part A*, *26*, suppl. 2, 217–248, 1979a.

Weisberg, R. H., A. M. Horigan, and C. Colin, Equatorially trapped Rossby-gravity wave propagation in the Gulf of Guinea, *J. Mar. Res.*, *37*, 67–86, 1979b.

Weisberg, R. H., J. J. Hickman, T. Y. Tang, and T. J. Weingartner, Velocity and temperature observations during the seasonal response of the equatorial Atlantic experiment at 0°N, 28°W, *J. Geophys. Res.*, *92*, 5061–5075, 1987.

Wilson, D., and A. Leetmaa, Acoustic Doppler current profiling in the equatorial Pacific in 1984, *J. Geophys. Res.*, *93*, 13,947–13,966, 1988.

Wyrtki, K., Lateral oscillations of the Pacific Equatorial Countercurrent, *J. Phys. Oceanogr.*, *8*, 530–532, 1978.

Yu, Z., Tropical instability waves in the Pacific Ocean: Their seasonal variation and asymmetry about the equator, Ph.D. dissertation, Nova Univ. Oceanogr. Cent., Dania, Fla., September 1992.

L. Qiao and R. H. Weisberg, Department of Marine Science, University of South Florida, 140 Seventh Avenue South, St. Petersburg, FL 33701. (e-mail: weisberg@marine.usf. edu)

(Received March 18, 1994; revised December 27, 1994; accepted January 23, 1995.)